Astron. Astrophys. 353, 691–706 (2000)

ASTRONOMY AND ASTROPHYSICS

The multiple system LHS 1070: a case study for the onset of dust formation in the atmospheres of very low mass stars⋆

Christoph Leinert[1], **France Allard**[2], **Andrea Richichi**[3], **and Peter H. Hauschildt**[4]

[1] Max-Planck-Institut für Astronomie, Königstuhl 17, 69117 Heidelberg, Germany
[2] Centre de Recherche Astronomique de Lyon, Ecole Normale Supérieure, 46 Allée d'Italie, Lyon, 69364 France, Cedex 07
[3] Osservatorio Astrofisico di Arcetri, Largo Enrico Fermi 5, 50125 Firenze, Italy
[4] University of Georgia, Department of Physics and Astronomy and Center for Simulational Physics, Athens, GA 30602-2451, USA

Received 21 July 1999 / Accepted 8 November 1999

Abstract. LHS 1070 (other common name: GJ 2005) is a nearby multiple system consisting of very low mass red dwarfs. We present the results of WFPC2 photometry and FOS spectroscopy for the three optically resolved components of this system acquired during HST cycle 5. These show (1) absolute brightnesses corresponding to theoretical masses of 0.080–0.083 $M_\odot$ and 0.079–0.080 $M_\odot$ for the faint pair, depending mainly on their age and metallicity; (2) a saturation of the optical TiO and VO absorption bands typical of the onset of photospheric dust formation, and (3) emission lines typical of moderate chromospheric activity in only the two most massive components. Li I lines are not seen. But also all other lines of the alkali elements are remakably weak or even absent in the two faint companions B and C. This appears to be an effect of dust formation. Comparison of the observations with model spectra, which account for dust formation and for the resulting opacities, yields good agreement for solar metallicity and effective temperatures and gravities (in $\log$ cm/s^2) of 2950 K;5.3, 2400 K;5.5 and 2300 K;5.5 for the three components A,B and C, respectively. The existence of a fourth component, recently discovered in this system by HST Fine Guidance Sensor observations (Henry et al. 1999), has already been taken into account in the evaluation of the data for the main component. An effective temperature and gravity (in $\log$ cm/s^2) for the fourth component of 2500 K;5.3 would best be compatible with our data. Then, based on our analysis the three components C, B and D of LHS 1070, in this order, are the faintest stars within 20 pc of the Sun for which dynamical determinations of mass appear possible within a decade. The system LHS 1070 thus has the potential to be the most important source of information for probing the low mass end of the main sequence.

Key words: stars: atmospheres – stars: binaries: general – stars: fundamental parameters – stars: low-mass, brown dwarfs – stars: luminosity function, mass function

Send offprint requests to: Ch. Leinert (leinert@mpia-hd.mpg.de)

⋆ Based on observations with the Hubble Space Telescope, with additional observations obtained on the ESO-MPIA 2.2 m telescope on La Silla, Chile.

1. Introduction

With the number of known brown dwarfs and low mass stars of very late type ($>$ M8) rising, it has become clear that most of them should form a new spectral class, provisionally designated by the letter L. The TiO and VO bands upon which the spectral classification of M type stars are usually based are only weak or even absent in their optical spectra. Metal–hydride bands of compounds involving non-refractory elements (like CrH), and atomic resonance transitions of alkali elements such as the K I doublet at $\lambda 7666, 7699$Å, the Na I doublet at $\lambda 8183, 8195$Å, the Rb I lines at $\lambda 7800$Å and 7948Å, and the Cs I lines at $\lambda 8521$Å and 8944Å become prominent in these stars in proportion to their relative cosmic abundances (Martín et al. 1997, Kirkpatrick 1998, Tinney et al. 1998, Basri et al. 1999).

Atmospheric modeling has allowed to determine the fundamental reasons of such a change: the onset of dust grain formation in the photospheric layers (Tsuji et al. 1996a, 1996b; Allard et al. 1996; Allard 1998). Indeed, dwarfs with effective temperatures of less than 2600 K have outer photospheric layers cooler than 1500 K, i.e. well into the regime of dust grain formation from compounds such as corundum (Al_2O_3), calcium titenade ($CaTiO_3$) and other complex calcium silicates. This condensation gradually depletes their photosphere of gaseous TiO and various refractory elements, while leaving the alkali elements (Li, Na, K, Rb, and Cs) relatively undepleted. The greenhouse effect caused by the opacity of the dust particles also increases the temperature of the photosphere, partly dissociating important molecular absorbers such as water vapor and CO, not otherwised affected by the condensation processes. This explains the extremely red near-infrared colors ($J - K > 1.0$) of most of these objects.

It appears, however, that the same models cannot explain the spectral properties of still cooler dwarfs such as Gliese 229B (Oppenheimer et al. 1995, Nakajima et al. 1995) without assuming that most if not all of the dust grains (and with them the resulting greenhouse effect) have vanished from the photosphere, presumably by gravitational settling (Tsuji et al. 1996b, Allard et al. 1996). It is important to establish in which measure these processes also apply to late M and early type L

dwarfs. How good can the current models, without consideration of gravitational settling, reproduce the spectral properties of these dwarfs? Can we establish how much of the dust must have settled as a function of the mass along the L type spectral sequence?

The observational resolution of these questions is no simple task because of the natural dispersion of populations and hence gravities and metallicities among late-type dwarfs in the solar neighborhood, which would make it necessary to distinguish condensation effects from age and metallicity effects in these objects. Most stars showing the effects of dust formation for which spectra could be obtained are free-floaters of unknown mass and metallicity. In this respect, the LHS 1070 multiple system offers the advantage that all of its components presumably are of the same age and metallicity. In addition, apart from GJ 1245, the system LHS 1070 is the only one in the solar neighborhood comprising late M/early L type dwarfs immediately at the hydrogen burning limit for which dynamical masses can be determined. Accurate stellar parameters for this system therefore will provide a unique opportunity to better determine the end of the main sequence and the still poorly understood transition region between low mass stars and brown dwarfs, while yielding solid constraints for stellar models.

In this paper we present the first step of our spectral analysis of the LHS 1070 red dwarfs: the analysis of the optical spectral range using the HST FOS spectra and WFPC2 photometry of each of the three resolved components A, B, C, obtained with HST during Cycle 5. The optical spectral analysis should already give us most of the information on the distribution of dust and on the structure of the photospheres of these objects, and should best allow us to determine spectral type and to quantify their stellar parameters: effective temperature, surface gravity, metallicity. From the latter we can infer mass and radius by using theoretical stellar evolution models and assuming the age of the system.

In the following, we present in Sect. 2 the FOS and WFPC2 observations and in Sect. 3 the model atmospheres used in the analysis. In Sect. 4, we give magnitudes and we also classify the components according to current spectral classification criteria. A mass estimate of the components is drawn from the absolute magnitudes in Sect. 5, while the spectral analysis of the FOS spectra is presented in Sect. 6 where we also discuss the possible unresolved binarity of component A. We also derive the transformations necessary to convert the VEGAMAG photometry to the Johnson/Cousins system for very red dwarfs. These colour-dependent corrections are shown in the Appendix.

2. Observations and data reduction

The geometrical distribution of the three components of the system LHS 1070 discovered by speckle interferometry (Leinert et al. 1994) is shown in Fig. 1: component B is at 1.1″ north of component A, component C is again north of component B and has changed position from 0.27″ under position angle 329° to 0.36″ under position angle 38° between 1993 and 1998. This spatial closeness, and the large brightness difference to be expected between the primary and its companions at visible wavelengths, made the object a natural candidate for observations in space with the Hubble Space Telescope (HST). Late in 1995 we obtained HST photometry and spectroscopy, which enabled us to perform the present study of the object based on its appearance in the visible wavelength range.

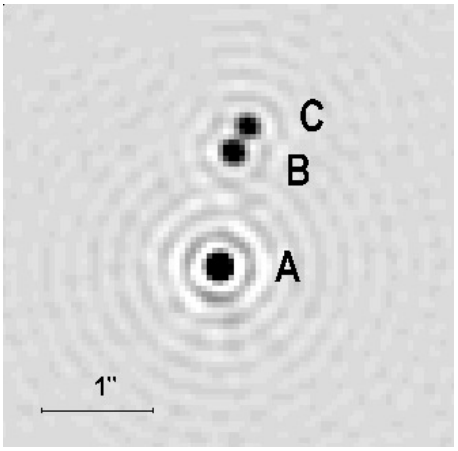

Fig. 1. Geometry of the system LHS 1070 at the time of the discovery of the companions B and C in July 1993 as seen at 2.2 μm.

Table 1. Integration times for WFPC2 photometry

Filter	Time (s)	Remarks
F439W	350	100 counts for component C
F555W	20	400 counts for component C
F675W	10	1 pixel saturated in component A
F814W	10	5 pixels saturated in component A
F656N	400	
F658N	300	
F673N	200	

The fourth component recently discovered by Henry et al. (1999) from observations with the HST Fine Guidance Sensor is a close companion to the main component A, separated by only ≈50 mas. With this additional component, LHS 1070 then is a quadruple system, one of the few known within 10 pc. For most of the following, however, we do not mention explicitly the fourth component but tacitly include it when discussing the measurements of the main component A.

2.1. WFPC2 photometry

Observations in the broad-band BVRI filters (F439W, F555W, F675W, F814W) and in three narrow-band filters around Hα (F656N, F658N, F673N) were obtained with the Wide Field Planetary Camera 2 (WFPC2) on July 14, 1995. To achieve the highest spatial resolution available (0.046″/pixel), the object image was positioned on the Planetary Camera chip. The circumstances of the different exposures are summarised in Table 1.

The photometric reduction falls into two parts: first, we derive the brightness of the components in the HST system, either

as equivalent flux (F_λ=constant, also expressed in STMAG magnitudes) or in magnitudes in the so-called VEGAMAG system. This is a comparatively accurate procedure, and these results are sufficient for a large part of the discussions. However, for comparison with other observations we also need BVRI magnitudes in the Johnson and Cousins systems. The necessary transformations constitute the second part of the data reduction.

For the *photometry in the HST system*, we rely on the pipeline calibration and flatfielding, remove bad pixels from the images, and do aperture photometry in MIDAS and photometry with DAOPHOT (including PSF fitting) on the three resolved components, in each case with a radius of 4 pixels. As described in the two basic papers by Holtzman et al. (1995a, 1995b) we correct for aperture size, detector gain, and photometric zero point, but we use the numerical values as given in the HST Data Handbook, Version 3 of October 1997, in Table 28.1 on page 28.7. No correction for geometrical distortion was needed. Some correction for a slight saturation of the red images of component A was necessary (see Table 1). For this, we made use of the WFPC2 point spread function (PSF) library available at the HST Web site. Unfortunately, at the time of our data analysis, suitable PSF profiles were available only for the F814W filter. In this case, a total of eight stellar images, with total counts comparable to LHS 1070 A and in a similar position on the WFPC2 chip, were used to build an average PSF. This was fitted to the outer, unsaturated parts of the F814W data for LHS 1070 A to estimate the flux in the 5 saturated pixels. An error of 0.05 mag was estimated for this procedure from the scatter obtained when using different library data. For what concerns the filter F675W, we used a similar approach but we had to resort to a comparison with our own data for filter F675N, which were unsaturated and at a wavelength very close by. The restriction that we could only use one PSF in this case was balanced by the fact that we needed to correct one pixel only.

While all these corrections are fairly well defined, the losses due to not perfect charge transfer efficiency (CTE) involved judgment. We started from the report by Whitmore & Heyer (1997), but judged that the formulae given by them have too strong a dependence on background for strong signals and exaggerate the correction if extrapolated to the small background readings occuring with short integration times. Therefore we referred not only to their equations (No. 2a and No. 2c) but also to their graphical summary of their measurements in their Fig. 9 (not extrapolating the measured effects), taking the average of the two values obtained in these two ways as representative for the CTE losses in the Y direction on the chip. The resulting total CTE corrections, shown in Table 2, are larger than those we had extrapolated from the papers of Holtzman et al. (1995a, 1995b), notably in V (x2.1), R (x2.9) and I (x2.0). We do not think that the corrections derived as described can be more accurate than to 1/3 or 1/4, and where formally the errors of a measurement came out smaller, we increased them accordingly. If anything, we may have overcorrected for CTE losses. In this case, the true brightnesses of the components of LHS 1070 would be smaller by a few percent than the values given in this paper.

Table 2. Adopted corrections for CTE losses (%)

Filter	component A	component B	component C
F439W	5.1 ± 2.0	8.9 ± 2.5	10.4 ± 3.0
F555W	6.9 ± 3.0	11.5 ± 3.1	12.5 ± 3.5
F675W	6.1 ± 2.4	10.0 ± 2.5	10.4 ± 3.0
F814W	4.1 ± 1.5	5.4 ± 2.0	5.7 ± 2.0
F656N	4.4 ± 1.5	7.8 ± 2.5	8.3 ± 2.5
F658N	5.5 ± 2.0	9.5 ± 2.5	9.8 ± 2.5
F673N	5.2 ± 2.0	8.6 ± 2.5	8.8 ± 2.5

The *transformation to the Johnson/Cousins BVRI system* are not trivial because the synthetic and empirical colour term equations given in the papers by Holtzman et al. (1995a, 1995b) have to be extrapolated quite a bit for the very red components of the system LHS 1070. It would need WFPC2 observations of very red objects with known BVRI values to improve reliably on these transformation for the application to red objects. For the time being, extrapolation on the basis of the different transformation equations would lead to differences in the predicted colour corrections of up to 0.5 mag (even 0.8 mag in B) for the reddest component of the system. These uncertainties are so large that we considered this approach as unacceptable for our purpose, and we had to find a different solution. The problem of relating HST photometry to standard "ground-based" systems for very red objects has not been covered sufficiently in the literature as yet, and for this reason we regard it worthwhile to describe explicitly our procedure and the related calibration diagrams. This description is given separately in the Appendix. As a short summary, we mention here that we have used the HST Synphot package running under IRAF and its library of stellar spectra to calculate the magnitude differences between the Johnson/Cousins and the HST VEGAMAG systems for a large number of stars with late-type spectra. From these, we have created color-color plots which have been used to estimate the colour corrections needed in the case of the components A, B, and C of LHS 1070.

The resulting fluxes and BVRI magnitudes are summarised in Table 3 in Sect. 4.

2.2. FOS spectrophotometry

The spectroscopic observations with the Faint Object Spectrograph (FOS) of the HST were obtained on October 29, 1995 during ten spacecraft orbits. The acquisition was done on the brightest component, LHS 1070 A, in four steps using the procedure "ACQ/PEAK" with progessively smaller apertures (3.7″, 0.86″, 0.26″) and step sizes (0.17″ and 0.052″ on the smallest diaphragm). The offsets from the brightest component to components B and C was based, among others, on the relative positions determined from the WFPC2 exposures. The acquisition was succesful in that separate spectra could be taken of components B and C (separated by 0.4″ during the time of the FOS observations) through the 0.26″ diameter aperture, and in that the signal loss due to imperfect centering into this small

aperture was only 5% - 10%, based on the comparison with the WFPC2 images (see Table 3). Spectra were taken with the red channel of the FOS spectrograph, both with high and low resolution, yielding results in the ranges 456.9 nm - 681.7 nm (grating G570H, 0.11 nm/pixel), 626.9 nm - 849.8 nm (grating G780H, 0.14 nm/pixel) and 354.0 nm - 707.4 nm (grating G650L, 0.61 nm/pixel). Note that the original spectral element size, the diode, is four pixels wide; the small pixel sizes were obtained by dithering within the exposure time in order to improve the spectral resolution, a standard feature of FOS observations. The actually achieved spectral resolution (FWHM) is about 3.75 pixels or 0.41 nm, 0.53 nm and 2.4 nm, respectively.

We relied on the flatfielding, calibration, bad pixel correction, background and dark current subtraction of the pipeline reduction. From the formulae given in the "Hubble Space Telescope Faint Object Spectrograph Instrument Handbook" (version 5.0, May 1994) we do not expect a disturbing influence by spectral straylight, nor by overspill from one component to the other, and these expectations appear to be born out by the comparison with the WFPC2 photometry (see Table 3). However, we obtained one recalibration with the latest calibration tables in August 1998, when we suspected that a depression over a few nm in the spectrum near 760 nm was due to inadequate calibration (it was). Apart from this correction and a resulting moderately increased brightness for components B and C longward of 700 nm, the original calibration and the recalibrated data were practically the same.

For comparison with model spectra it is important to cover continuously as large a part of the visible spectral range as possible, since this provides a strong constraint on effective temperatures. To this end we extended the spectra obtained with grating G570H to the red (using data from G780H) and to the blue (using data from G650L), by multiplying these spectra with a fitting factor determined in the overlap region. Typical values of this factor are 1.01 - 1.04. The results were continuous spectra for the three components running from 354 nm to 849 nm, with varying resolution along the spectrum. These constitute the main data set to be compared with the model atmospheres in Sect. 6.

The wavelength corresponding to a given pixel may be shifted for each exposure by a substantial fraction of a diode (4 pixels). This offset can be determined from features like emission lines and strong band heads. The wavelength shift due to the radial velocity of the system of -36 km/s (Basri & Marcy 1995) is small compared to these offsets, and the effects of orbital motion in the system by a few km/s are negligible.

2.3. Comparison of photometry and spectrophotometry

As a consistency check and a check on the photometric and spectrophotometric reductions, we integrated the component spectra obtained with FOS over the WFPC2 filter bandpasses (including system transmission) as available from STScI. For the I filter (F814W) we had to extend the observed spectra longwards to about 1.1 μm, which we did by using the "NextGen" models (Allard et al. 1997 and Hauschildt et al. 1999) with solar metallicity and $\log$ g = 5.0. Based on first fits to the FOS spectra (Leinert et al. 1998) we chose to do the extension with the $T_{\rm eff}$ = 2900 K model for component A, and with the 2500 K model for components B and C. The ratio of the average spectral fluxes F_λ resulting from the FOS spectra to the values of F_λ resulting from the WFPC2 photometry are given in Table 3 in parentheses with the flux values. For component A, observed in FOS with a larger diaphragm of $0\farcs86$ diameter, the photometry results reproduced within $\pm$2% for V, R and I, and within 6% for B, the most difficult band because of the low spectral fluxes. This agreement is quite satisfactory. For components B and C, the FOS fluxes are low by about 10%. This is not unexpected, when centering such faint objects into a diaphragm of only $0\farcs26$ diameter. The colours of the components are reproduced for each component with a rms difference of 0.03 mag, if we omit the most uncertain value (B-V for component C). In summary, this comparison leads us to accept both the WFPC2 photometric and the FOS spectrophotometric calibrations.

3. The model atmospheres

For the purpose of the present analysis, we have constructed a grid of cool plane-parallel model atmospheres in local thermodynamical and hydrostatic equilibrium, using the model atmosphere and radiative transfer code PHOENIX, version 10.7 (Allard et al., in preparation). The models cover the range $1500\,{\rm K} \leq {\rm T_{eff}} \leq 3000\,{\rm K}$, and include (i) the formation of over 600 gas phase species, liquids and crystals, and (ii) the opacities of Cu, Ni, Nb, Ti, and Fe crystals, of troilite (FeS), MnS, hematite (Fe_2O_3), magnetite (Fe_3O_4), ZrO_2, corundum and sapphire (forms of Al_2O_3), magnesium aluminium spinel $MgAl_2O_4$, enstatite ($MgSiO_3$), forsterite (Mg_2SiO_4), amorphous carbon, SiC, as well as a number of calcium silicates ($CaSiO_3$, Ca_2SiO_4, $Ca_2Al_2SiO_7$, $Ca_2MgSi_2O_7$, and $CaMgSi_2O_6$). The chemical equilibrium incorporates the complete series of liquids and crystals also studied by Sharp & Huebner (1990). For each grain species, a number density is calculated following the prescriptions of Grossman (1972) and using the free Gibbs energy of formation. We assume that the grains remain in equilibrium with the surrounding gas phase, and remain suspended at their condensation layer. The grain opacities are reconstructed from their polarizability spectra obtained in the laboratory from e.g. Begemann et al. (1997), and Dorschner et al. (1995), assuming an interstellar grain size distribution ($n(a) \sim a^{-3.5}$, $a = 0.025 - 0.25\mu$m; Mathis et al. 1977), spherical geometry of the grains, and using the Mie theory formalism (see also Alexander et al. 1998). Inclusion of the dust opacity thus does not introduce a new fitting parameter but is handled in a direct, physical way. Unfortunately, the necessary optical data are not available for all of the grain materials; this prevents to include the contribution to the opacity by these, usually less abundant, grain species. The models also present major differences in other aspects with previous versions such as the NextGen models (Allard et al. 1997, Hauschildt et al. 1999): we have used the new molecular opacities for TiO by Langhoff (1997) and Schwenke (1998), and recalibrated the astrophysical oscillator strengths

Table 3. Photometry of LHS 1070 and of its components

Wavelength range[1]	component A	component B	component C	LHS 1070
$B_{Johnson}$	17.17±0.05	20.57±0.07	21.48±0.11	17.10±0.06
F439W[2]	17.70±0.03	21.16±0.06	22.09±0.10	17.64±0.03
430.0 nm[3]	5.55×10^{-16}(1.060)	2.29×10^{-17}(0.924)[5]	9.74×10^{-18}(1.068)[5]	5.88×10^{-16}
$V_{Johnson}$	15.35±0.04	18.68±0.06	19.07±0.07	15.27±0.05
F555W[2]	15.40±0.04	18.69±0.06	19.07±0.07	15.31±0.04
539.7 nm[3]	2.52×10^{-15}(0.983)	1.21×10^{-16}(0.938)[5]	8.57×10^{-17}(0.878)[5]	2.73×10^{-15}
$R_{Cousins}$	13.63±0.04	16.30±0.05	16.65±0.05	13.48±0.04
F675W[2]	13.58±0.03	16.36±0.05	16.70±0.05	13.44±0.03
669.7 nm[3]	7.04×10^{-15}(0.992)	5.45×10^{-16}(0.948)[5]	3.97×10^{-16}(0.906)[5]	7.98×10^{-15}
$I_{Cousins}$	11.66±0.04	14.01±0.05	14.43±0.05	11.47±0.04
F814W[2]	11.61±0.03	13.76±0.04	14.19±0.04	11.38±0.03
792.4 nm[3]	2.57×10^{-14}(0.983)	3.56×10^{-15}(0.986)[5]	2.40×10^{-15}(0.932)[5]	3.17×10^{-14}
656.3(2.2) nm[4]	8.80×10^{-15}±3%	6.05×10^{-16}±4%	3.04×10^{-16}±5%	9.71×10^{-15}±3%
659.1(2.9) nm[4]	6.24×10^{-15}±3%	3.55×10^{-16}±4%	2.51×10^{-16}±5%	6.85×10^{-15}±3%
673.2(4.7) nm[4]	3.72×10^{-15}±3%	3.02×10^{-16}±4%	2.46×10^{-16}±5%	4.27×10^{-15}±3%
F439W - F555W	2.30±0.04	2.47±0.07	3.02±0.10:	2.33±0.04
B_J - V_J	1.82±0.05	1.89±0.08	2.41±0.11:	1.83±0.05
F555W - F675W	1.82±0.04	2.33±0.06	2.37±0.07	1.87±0.04
V_J - R_C	1.72±0.05	2.38±0.06	2.42±0.07	1.79±0.05
F555W - F814W	3.79±0.04	4.93±0.05	4.88±0.06	3.93±0.04
V_J - I_C	3.69±0.05	4.67±0.06	4.64±0.07	3.80±0.05

[1] effective wavelengths from Holtzman et al. (1995b).
[2] magnitudes are in the HST VEGAMAG system.
[3] fluxes in erg cm^{-2} s^{-1} $Å^{-1}$. The number in parentheses gives the flux ratio FOS/WFPC2 over this filter band.
[4] bandwidth is given in parentheses, taken from the Wide Field and Planetary Camera 2 Handbook, Version 4.0, June 1996.
[5] about 10% loss in FOS flux is caused by centering into the $0''.26$ diameter diaphragm.

of the CaH, and VO bands so as to fit the observed features of LHS1070A with the new background TiO opacities. Since LHS1070A, with an effective temperature well above 2600K, is free of dust grains, it appears to provide an appropriate calibration of molecular absorption bands lacking independent oscillator strength measurements. We have **not** used the new H_2O line lists by Partridge & Schwenke (1997), and have rather retained the water vapor lines by Miller & Tennyson (1994) as in the NextGen models. The two lists yield very different results for the infrared spectral distribution of these stars, but using one or the other does not affect the optical spectra and the results presented here. We will discuss the infrared spectral distribution and the various water vapour opacity sources available in a subsequent paper.

Because our new models rely on the TiO line list computed by the NASA AMES team, on the water vapor lines by Miller & Tennyson and include dust effects, we have named them the "AMES-MT-Dusty" model series. Preliminary versions of these models have already been compared to spectra of late-type dwarfs and brown dwarfs by Leggett et al. (1998), Ruiz et al. (1998), Kirkpatrick et al. (1999a), Tinney et al. (1998), and Basri et al. (1999), and have shown a remarkable improvement of the model predictions for the near-infrared spectral distribution and colors of these objects. The present analysis will allow to estimate the suitability of these models to reproduce the optical spectroscopic properties of red dwarf stars.

4. Results

4.1. Brightness and colour of the components

Brightness and colour of the three resolved components of LHS 1070 and of the integrated system as well are given in Table 3 both in the HST VEGAMAG and the Johnson/Cousins BVRI system. To avoid confusion between systems, we identified the WFPC2 bands by their filter names. In addition, the table also gives equivalent fluxes F_λ at the effective wavelengths of all WFPC2 bands, including the narrow-band filters. These fluxes have the same errors as the VEGAMAG brightnesses, to which they are essentially equivalent. The numbers added in parantheses to the fluxes in case of the broad-band filters show by which factor the fluxes of the FOS spectra differ from the photometrically obtained average values of F_λ over the filter bands.

For comparison, we note that the B-V and V-I values for the well-observed nearby M dwarfs VB8 (M7 V) and VB10 (M8 V)

Table 4. LHS 1070 system photometry compared to ground-based results

Filter band	WFPC2 (1995)	ESO (1994/1996)	Leggett (1992)
$B_{Johnson}$	17.10±0.06	17.25±0.10	
$V_{Johnson}$	15.27±0.05	15.43±0.05	15.42
$R_{Cousins}$	13.48±0.04	13.49±0.02	13.71
$I_{Cousins}$	11.47±0.04	11.34±0.06	11.56

have been measured as 2.20, 4.56 and 2.13, 4.70, respectively (Leggett 1992). Because of the similarity in these colours, we expect that components B and C fall into the same range of effective temperatures as do these two dwarfs.

4.2. Comparison with ground-based photometry

In Table 4 we compare the WFPC2 photometry for the system LHS 1070, transformed to the Johnson/Cousins UBVRI system, with the results given by Leggett (1992) and with photometry we obtained in November 1994 (BVR) and in January 1996 (I) from ESO, La Silla. At ESO, the T Phe and PG 0231+051 fields from Landolt (1992) and the E2-region from Graham (1982) were used for brightness standards, and these fields contain a large enough spread in B-V values of the standards to allow reasonable colour corrections. There is disagreement on the order of 0.1 mag between the different photometries. This may point to the fact that photometry of very red objects is not an easy task. Or it may mean that, for reasons we are not aware of, our HST based photometry led to an overestimate of brightnesses. Like in the case of the corrections for CTE losses, we then would again have to conclude that the true brightnesses of the components of LHS 1070 are fainter by several percent than given in this paper.

4.3. Spectral classification of the components

The spectral classification of the components of LHS 1070 was based on the wavelength range 640 nm - 850 nm. We determined spectral types from the VO absorption band at 744.5 nm according to the VO ratio defined by Kirkpatrick et al. (1995), from the pseudocontinuum gradient between 756 nm and 825 nm according to the ratio PC3 defined by Martín et al. (1996), and in particular by comparison with standard spectra and consistently typed late star spectra from Kirkpatrick et al. (1991, 1995), Henry et al. (1994), Tinney et al. (1998) over all of the wavelength range from 640 nm to 850 nm. The comparison was done by overlaying the FOS results to the published spectra. The spectral types resulting from the ratios and the adopted classification are shown in Table 5. Component A has a spectrum almost identical to Gliese 65A (M5.5V), LHS 3339 (M5.5V) and in particular G 208-45 (M6V). Similarly, component B resembles very much the spectra of TVLM 513-46546 (M8.5V) and BRI 1222-1222 (M9V), but in particular to J0020-4414 (M8V) and J2146-2153 (M9V), and it is less blue than some of the M9

Table 5. Spectral types of the components of LHS 1070

Component	VO ratio	Type from VO	PC3 ratio	Type from PC3	Adopted, from comparison to standards
A	1.023	$M6^+$	1.40	M6.3	M5.5-6 V
B	1.141	M9	2.25	M9.4	M8.5 V
C[1]	1.142	M9	2.64	M9.6	M9-9.5 V
	1.152	M9	2.46	M9.6	
BC	1.090	M8	2.40	M9.6	M8.5 V

[1] two spectra available for component C

stars presented in the references. The spectrum of component C, with its comparatively weak VO band and comparatively high 850 nm pseudocontinuum has no exact match in the spectra mentioned above, LHS 2065 (M9) and PC 0025+447 (M9.5V) giving the best approximations. The combined spectral type for components B and C is also given since in many observations these components will not be resolved.

Within the new classification scheme for L dwarfs proposed by Kikpatrick et al. (1999a), component C would be assigned the spectral type L0, based on the shape of the VO band at 745 nm and the strengths of the K I and Rb I lines longward of it.

5. Mass estimates from absolute magnitudes

5.1. Absolute magnitudes

The parallax of LHS 1070 (alias GJ 2005) is given as 0.1353±0.0121″ (7.4±0.7 pc) in the 4th version of the General Catalogue of Trigonometric Stellar Parallaxes (van Altena et al. 1995), a value which is considered uncertain because of the presence of the B, C, and D components. Work on an improved parallax measurement is in progress (P. Ianna, private communication). For this paper we therefore determine the distance to LHS 1070 from a best fit to its spectrum, with a resulting distance of 8.8 pc, larger at the 2σ level. Once a reliable new parallax is available, this value may have to be revised - downwards or upwards. For most of this paper, the 2σ discrepancy is not important. For the absolute magnitudes, where it matters most, we give in Table 6 the results for both values of the distance. The errors are mainly determined by the error in the parallaxes.

5.2. Resulting photometric mass estimates

Photometric estimates of the mass of the components can be obtained both from empirical relations and from brightnesses predicted by stellar interior models when coupled to model atmospheres. The various estimates are summarised in Table 7.

For the *empirical mass estimates* we used the mass-M_V relationship of Henry et al. (1999) as well as the near-infrared counterparts of it (Henry & McCarthy 1993). We took the visual brightnesses from Table 6 and the near-infrared values from Leinert et al. (1994). For the *mass estimates from stellar models* we used the tabulation by Baraffe et al. (1998, 1999) for solar

Table 6. Absolute magnitudes of the components of LHS 1070

Wavelength band	Component A[1] at 7.4 pc	Component A[1] at 8.8 pc	Component B at 7.4 pc	Component B at 8.8 pc	Component C at 7.4 pc	Component C at 8.8 pc
$B_{Johnson}$	17.82±0.16	17.45±0.11	21.22±0.17	20.85±0.12	22.13±0.19	21.76±0.15
$V_{Johnson}$	16.00±0.16	15.63±0.11	19.33±0.16	18.96±0.12	19.72±0.17	19.35±0.12
$R_{Cousins}$	14.28±0.16	13.91±0.11	16.95±0.16	16.58±0.11	17.30±0.16	16.93±0.11
$I_{Cousins}$	12.31±0.16	11.94±0.11	14.66±0.16	14.29±0.11	15.08±0.16	14.71±0.11
F439W	18.35±0.15	17.98±0.10	21.81±0.16	21.44±0.12	22.74±0.18	22.37±0.14
F555W	16.05±0.16	15.68±0.11	19.34±0.16	18.97±0.12	19.72±0.17	19.35±0.12
F675W	14.23±0.15	13.86±0.10	17.01±0.16	16.64±0.11	17.35±0.16	16.98±0.11
F814W	12.26±0.15	11.89±0.10	14.41±0.16	14.04±0.11	14.84±0.16	14.47±0.11

[1] includes the unresolved companion D

Table 7. Component masses [$M_\odot$] estimated from photometry[1]

Component	Empirical relations[2] [M_V]	Empirical relations[2] [M_J,M_H,M_K]	Models ([Fe/H]=0, age = 5 Gyr)[3] [M_{F555W}]	Models ([Fe/H]=0, age = 5 Gyr)[3] [M_{F814W}]
A[4]	0.100-0.105	0.097-0.113	0.098-0.101	0.101-0.109
B	0.069-0.071	0.059-0.069	0.080-0.081	0.081-0.083
C	0.067-0.069	0.054-0.063	0.079-0.080	0.079-0.080

[1] The range in masses refers to the possible range in parallax.
[2] Henry et al. (1999), Henry & McCarthy (1993).
[3] Baraffe et al. (1998).
[4] The close companion D to component A is not mentioned explicitely, since it is too faint to increase brightness and deduced mass to a noticeable amount, except perhaps for the estimates based on the near-infrared brightnesses.

metallicity and an age of 5 Gyr, which includes tables giving the brightness of low mass objects as function of mass for various spectral bands, which tabulations are also available for the HST WFPC2 filter bands (see Sect. 6.2). The uncertainty of the transformation to the UBVRI system therefore only enters the empirical estimates based on M_V. Visual brightness has such a strong dependence on mass for these objects that this uncertainty, which is much smaller than the effects of uncertainty in parallax, is not important here. For the same reason, the estimates also depend little on the detailed assumption on age. For an assumed age of 1 Gyr, they would remain unchanged for component A, while the estimated masses for B and C would decrease by 0.002 $M_\odot$. Decreasing the metallicity by a factor of 3 would decrease the mass of component A by 0.007 $M_\odot$ and let the components A and B almost unchanged (+0.002 $M_\odot$) The substellar masses resulting from the empirical determinations for components B and C are an interesting result for objects with apparently normal stellar spectra, but one has to keep in mind that their derivation included extrapolation to slightly beyond the limits to which the applicable relations had been empirically defined. These results therefore are somewhat uncertain. However, it should be noted that the three components C, B and D of LHS 1070 (the latter with $M_V = 18.4 \pm 0.3$, Henry, private communication), in this order, are the faintest stars within 20 pc of the Sun (judged by M_V), for which dynamical determinations of mass appear possible within a decade (orbital period less than 20 years). This makes LHS 1070 a truly remarkable system, which has the potential to be the most important source of information for probing the properties of the low mass end of the main sequence.

6. Analysis of the optical spectra

Before entering the detailed and extended discussion, let us summarise the results. We have for

component A T_{eff} = 2950 K, $\log g$[cms^{-2}] = 5.3 ± 0.2
no effects of dust;
component B T_{eff} = 2400 K, $\log g$[cms^{-2}] = 5.5 ± 0.5
strong effects of dust;
component C T_{eff} = 2300 K, $\log g$[cms^{-2}] = 5.5 ± 0.5
strong effects of dust;
component D T_{eff} = 2500 K, $\log g$[cms^{-2}] = 5.5 ± 0.5
(values uncertain).

The effective temperatures above give the best representation of the observations with assumption of a distance of 8.8 pc. For smaller distances, lower effective temperatures would result, by about 100 K per 1 pc change in distance. A reliable parallax and additional infrared observations are needed to resolve this uncertainty. These results were obtained assuming solar metallicity and an age of the system LHS 1070 of roughly 5 Gyr, which choices will be justified below.

6.1. Age of the system

From high resolution spectra obtained at the Keck telescope Basri & Marcy (1995) determined the space velocity of the system LHS 1070 perpendicular to the galactic plane as W =

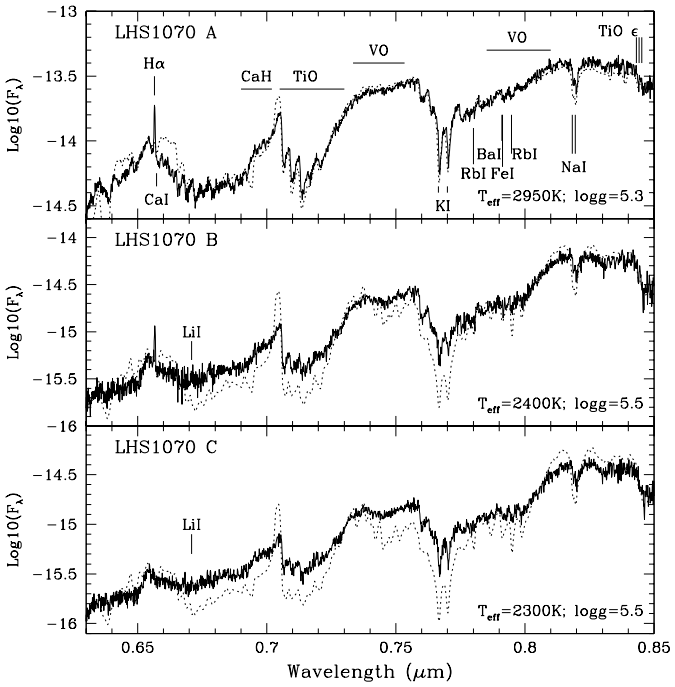

Fig. 2. Red part of the FOS spectra of the three resolved components (solid lines), compared to synthetic spectra taken from the AMES-MT-Dusty model series (dotted). The model spectra have been converted to absolute fluxes at the position of the observer (in erg cm^{-2} s^{-1} Å^{-1}) based on stellar radii taken from the corresponding evolution models (Baraffe et al. 1998,1999), and assuming a distance for the system of 8.8 pc. The strength of the TiO λ7140Å and the VO λ7430Å absorption bands decrease or only slightly increase from component A to the much cooler components B and C. This saturation is a clear sign of dust formation in the photospheres of the two faint companions.

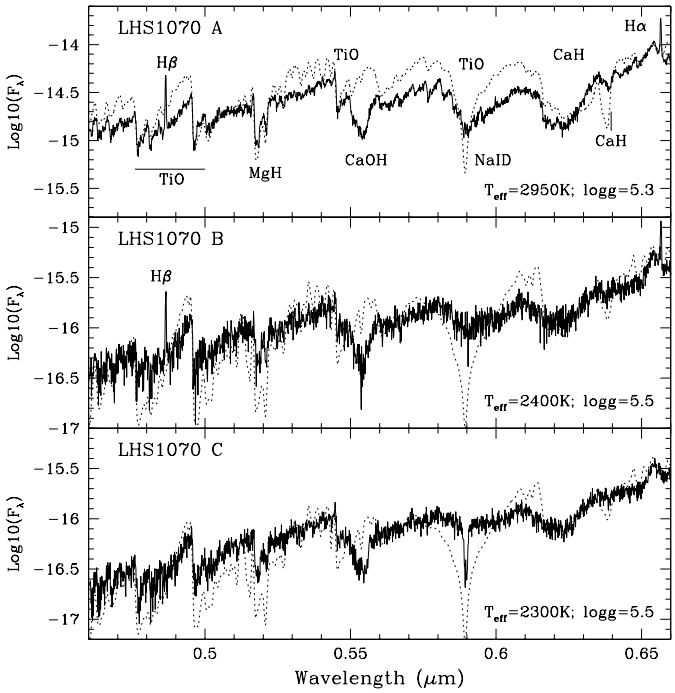

Fig. 3. Same as Fig. 2 for the visual spectral range. We note the near-absence of the wings of the Na I D λ5891,5897Å lines in the two companions. In the primary spectrum and in component B the Na I D line core appears filled in, perhaps by chromospheric emission.

35 km/s. This puts the system kinematically into the old disk population and makes it probable that its age is several Gyr. For the purposes of the following discussions, in this range the exact value of the age does not matter, and we assume it to be equal to 5 Gyr. Even in the case of photometric mass estimates, where the age might matter most, the effect of a factor of five in assumed age is small (see Sect. 5.2).

6.2. Estimates of stellar parameters

The preliminary fits to the observed spectra of components A, B and C, based on the *grainless* NextGen models presented in Leinert et al. (1998) had a problem: for all three of the components, the models, when fitted to the observations in the red part of the spectrum, predicted substantially higher fluxes than observed for the visible and blue regions. This indicated that the fainter components probably are the site of dust formation which, by the additional opacity and by additional heating of the outer atmospheric layers, reduces the opacities in the VO, TiO, and H_2O bands. In this situation, the grainless models, predicting only a steady increase of molecular band strengths with decreasing temperature up to saturation, could only overestimate the effective temperatures.

6.2.1. Effective temperatures

Our best fits to the "high resolution" spectra of the components of LHS 1070 are shown for the red part of the spectrum in Fig. 2, for the green part of them in Fig. 3. In addition, Fig. 4 shows the same model fits for components B and C over the full available wavelength range of 350 nm - 850 nm, which however is only covered at low resolution for wavelengths shorter than 460 nm.

It should be noted that in these figures the synthetic spectra, otherwised expressed in units of the stellar surface flux density (erg/s/cm^2/Å), have been converted to "observed" absolute fluxes (i.e. multiplied by the dilution factor $[r/d]^2$) using the radii "r" provided by an unpublished updated version of the $T_{\rm eff} - \log g$ - radius relation given by the interior models of Baraffe et al. (1998, 1999), and assuming an age of 5 Gyr for the LHS1070 system. These updated interior models have been computed using the atmospheric (T,$P_{\rm gas}$) structure of the "dusty" atmosphere models described in this paper and are therefore completely consistent with the present models. Being equivalent to the observed quantities, the model fluxes then imply automatically the relative brigthness of the components, and thus constrain further the choice of the adequate atmospheric parameters for the components. Adopting a distance of 8.8 pc, we found that the models provide an excellent match to the spectral features, and a reasonable fit to the "continuum" distribution and brightness of the primary star, LHS1070A (with part of the agreement due to the fact that the *total* strength of the CaH and VO bands has been calibrated on this spectrum). This result in-

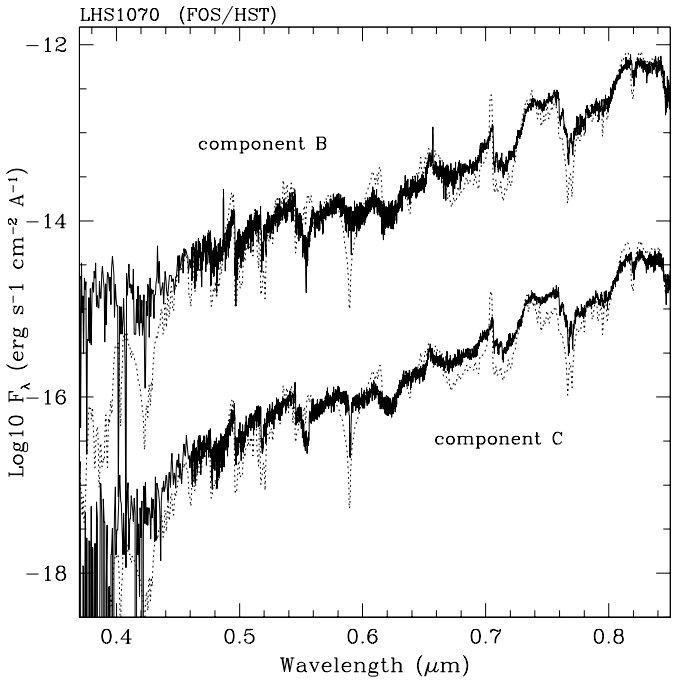

Fig. 4. Overall observed FOS spectrum of components B and C (solid lines) compared to the best fitting models (dotted). The FOS spectra shown are combined from the spectra given in Figs. 2 and 3 and have been extended by the low resolution FOS spectra at the blue end. They show a remarkable absence or striking weakness of the CaI λ4227Å transition. We observe that the selected models provide an acceptable match to the overall spectral distribution of the continuum throughout the covered wavelength range. A distance of LHS 1070 of 8.8 pc has been used to fix the absolute flux level, and the spectrum of component B has been shifted upwards by adding 2 to the logarithm of its flux.

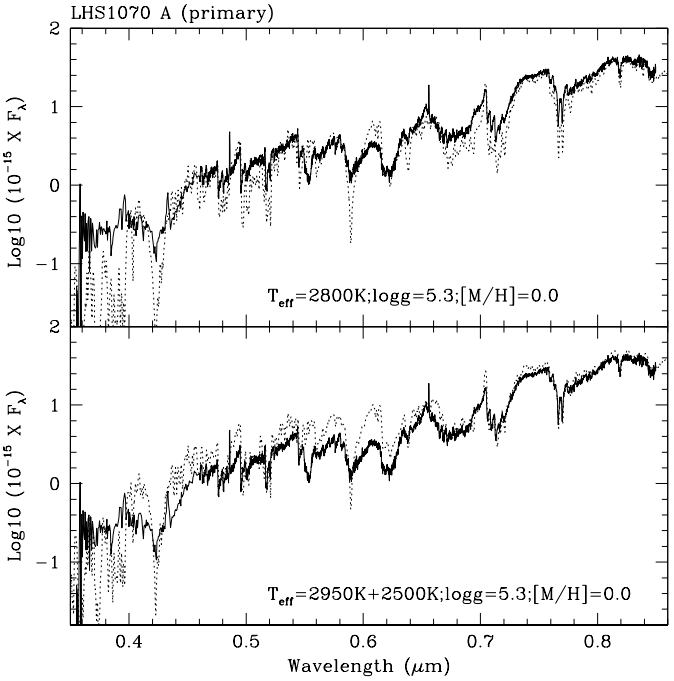

Fig. 5. One- and two-component model fits to the overall observed spectrum of the primary star (solid line). As in Fig. 4, the high resolution FOS data have been extended by the low resolution spectrum at the blue end. Note the strong emission at Hγ as well as the pronounced absorption feature of the Ca I λ4227Å transition. Upper panel: while Figs. 2 and 3 show the model best reproducing the spectral features ($T_{\rm eff}$ = 2950 K, $\log g$ = 5.3 g s^{-2}), the single component model shown here (dotted) gives the best fit to the overall spectral slope. A distance of 7.3 pc has been used to fix the absolute flux level. Lower panel: two-component model, adding a cool companion ($T_{\rm eff}$ = 2500 K, $\log g$ = 5.5) to the primary ($T_{\rm eff}$ = 2950 K, $\log g$ = 5.3 g s^{-2}). Since the brightness ratio of the two objects amounts to a factor of 10 and more, the composite spectrum (dotted) is very similar to the one-component model used in Figs. 2 and 3. A distance of 8.8 pc has been assumed.

creases our confidence in the general reliability of the models, in a regime where atmospheric dust is not yet important.

The best fits in Figs. 2 and 3 were not selected to the same criterion. For component A, where the spectrum in the green part might be influenced by component D, we put the weight on a good reproduction of atomic and molecular features in the red part of the spectrum, which succeeded quite well. For components B and C, a good representation of the general spectral slope was considered most important. Here, the difficulty to fit the atomic lines simultaneously is obvious and makes these lines unsuitable as indicators of effective temperature. This point will be discussed further in Sect. 6.2.3. We first now look at the spectra of the two companions.

Clearly, the new "dusty" models are now quite different for components B and C than the earlier grainless models, and above all fit the blue part of the spectra *much* better. This improvement against the order of magnitude mismatch for dust-free models can best be judged from Fig. 4. For the spectral features, the important effect is that the grains, in particular $CaTiO_3$, have depleted TiO and CaH from the gas and reduced the strength of their emerging absorption bands. In general, the models appear to reproduce this behavior adequately. However, the strength of the VO $(B\text{-}X)_{01}$ bandhead near 740 nm is overestimated by the cool dusty models. With the VO and CaH bands fitted to reproduce the primary's features, the overestimation increases from B to C, i.e. with decreasing temperature, and it continues doing so for effective temperatures around 2000 K (see Fig. 7) below), while the TiO feature at 705 nm is better represented in the very cool, very dusty models. This suggests that further lowering the effective temperature does not solve the problem but that some important opacity source still may be missing in our models (see also Sect. 6.2.3).

For these reasons, we consider the effective temperatures of 2400 K and 2300 K used for the fits in Figs. 2 - 4 as realistic estimates for the temperature of components B and C. As with component A, the internal error of $T_{\rm eff}$ is estimated to $\pm$100 K. This estimate does not yet include the systematic effects mentioned at the beginning of this section, like the uncertainty in parallax or in the mass-radius-effective temperature relation, which may be of the same order.

6.2.2. Component D and the effective temperature for component A

From the point of view of spectral fitting it is an unfortunate complication that component A should have D as close companion. An independent confirmation of the existence of this fourth component and a measurement of the brightness ratio in a number of wavelength bands in the visual spectral region are highly desired.

For the time being we can only check whether a cool companion like component D is needed to adequately represent the observed spectrum A - the fit in Figs. 2 and 3 shows some excess in the blue part of the spectrum. Alternatively, Fig. 5 shows in its upper panel that a reasonable overall spectral fit can also be obtained with *one* object of T_{eff} = 2800 K. However, the atomic lines and molecular features clearly get less well reproduced, and the needed distance of 7.3 pc is by 20% smaller than the value of 8.8 pc inferred for components B and C. In the lower panel, a composite model, adding a cool companion to the model used for the primary in Figs. 2 and 3, is compared to the data. The atomic lines are now again fitted well. The excess in the blue is very nearly the same as for the original single-component model with T_{eff} = 2950 K, since the much cooler companion contributes little to the total flux. We do not need a cool companion to obtain reasonable fits to the spectrum of component A, but we cannot exclude the existence of such a companion either. For aesthetic (fit of atomic and molecular features) and economical reasons (same distance resulting as for components B and C) we estimate the effective temperature of component A to 2950 K, with an uncertainty of +50K -150K. Component D – if it gets finally confirmed – should not be hotter than the temperature of 2500 K used in the composite model, with an estimated uncertainty of $\pm$100 K.

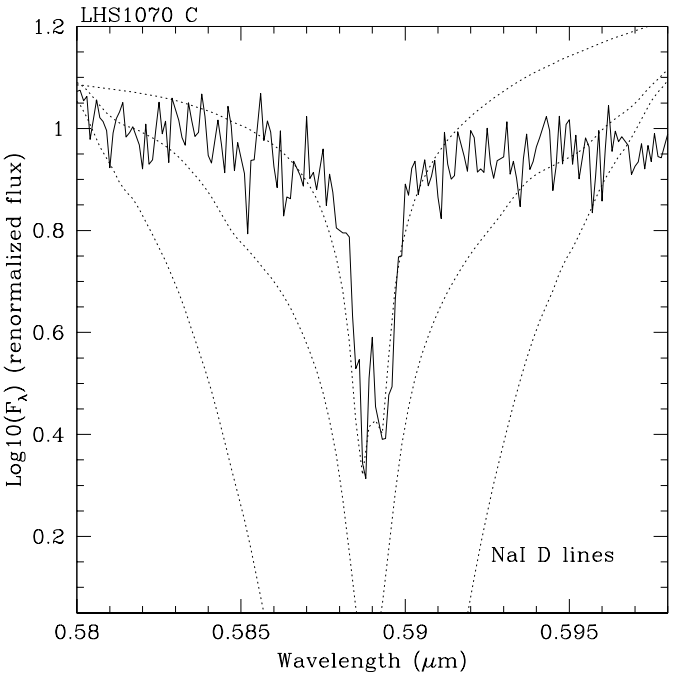

Fig. 6. The NaI D lines as observed in the faintest component C of the system (full line) are compared to models with increasing content of dust (dotted lines). The model predicting the strongest sodium line is a $T_{\rm eff}$ = 2300K model with $\log g$=5.5, and solar elemental abundances, where dust opacities are ignored but condensation of refractory elements to dust particules is included. The model just above is produced assuming the same atmospheric parameters but including all dust opacities. And the model matching best the observed feature is a cooler, higher gravity model including all dust ($T_{\rm eff}$ = 2050K model with $\log g$=6.0, and solar elemental abundances) intended to exaggerate the effects of dust in the atmosphere on the line profile. The fluxes of the models are scaled to match the continuum bluewards of the lines.

6.2.3. Gravity

The model atmospheres of M dwarf stars predict that, under an increased gravity, the pressure broadening (Van der Waals) of line profiles is enhanced, as well as the strength of the MgH absorption bands near 520 nm, and of the CaH bands near 620 nm, 640 nm, and 700 nm. However the CaH molecular bands were adjusted in their oscillator strengths, and as a result, cannot be used for the determination of gravity. We therefore determined gravity from atomic line profiles in this work. As with the effective temperatures, a clear answer is easier to obtain for the main component than for the companions.

In the case of the primary star, we found a very good agreement of the present models with the K I $\lambda 7665, 7699$Å and Na I $\lambda 8183, 8195$Å doublet profiles, with $\log g = 5.3 \pm 0.2$ (see Fig. 2). The presence of a cool companion would not improve the fits but not be much of a problem either since it would only contribute $\approx$10% to the flux at these wavelengths. The given value of $\log g$ is in close agreement with the predictions of $\log g \approx 5.2$ from interior models (Baraffe et al. 1998) for the effective temperature determined in the previous section (2950K) and solar metallicity at 5 Gyr. We feel therefore confident that the handling of Van der Waals broadening adopted in the model atmospheres code PHOENIX (see e.g. Schweitzer et al. 1997 for details) is adequate for these lines, despite current uncertainties in the Van der Waals damping constants for non-hydrogenic species. Please note that the Na I D lines at λ5891,5897Å usually also provide strong gravity and metallicity indications, but these lines show also a strong sensitivity to both dust formation and chromospheric emission which precludes their use for parameter determination in this case (see also Sect. 6.3).

In the faint pair (components B and C) we note the absence of photospheric Na I D and Ca I 4227 Å absorption lines (or at least of their pressure-broadened wings, see also Sect. 6.3), and the weakness of the K I $\lambda 7665, 7699$Å doublet. This is a behavior that has not yet been observed in the cooler L dwarfs (see Kirkpatrick 1998, Tinney et al. 1998, Basri et al. 1999). Can metal depletion by condensation into grains explain this effect? Calcium condenses abundantly to grains mainly via $Ca_2Al_2SiO_7$, $CaMgSi_2O_6$, $Ca_2MgSi_2O_7$, $CaSiO_3$, and $CaTiO_3$ and the current "dusty" models suggest that this occurs in the Ca I 4227 Å line forming region for these effective temperatures. Indeed, the models show a very weak Ca I 4227 Å line, but predict strong lines of Cr I near that wavelength, which appear as a broad ab-

sorption feature in the model spectra shown in Fig. 4. But a similar absorption feature does not appear in the low resolution spectra of B and C. Sodium on the other hand, does not condense before $T_{\rm eff} = 1900$ K, and even then only marginally via a trace liquid $Al_3F_{14}Na_3$ that cannot deplete sodium significantly from the gas phase. And potassium does not condense at all until even lower effective temperatures.

Condensation alone cannot therefore be responsible for the weakness of atomic lines observed in the two faint dusty companions. But dust absorption and scattering in the atmosphere causes a heating of the photospheric layers which can probably explain this behavior. To demonstrate the effect of dust heating upon the strength of atomic lines in these atmospheres, we show in Fig. 6 three models representing increasing effects of dust: one in which the condensed material is removed artificially from the atmosphere, one treating the dust formation as outlined above in Sect. 3, and one where dust formation and opacity effects have been exaggerated by artificially choosing a low effective temperature (2050 K) and a high atmospheric pressure ($\log g$ = 6.0). From this comparison we conclude that the presence of dust in the atmospheres of companions B and C may be responsible for the extreme weakness of the alkali lines observed. Models of increasing gravity cause more grains to form, and atomic lines to become weaker as the atmosphere becomes more opaque. Decreasing effective temperature in this regime (2600K down to 1700K) has similar effects. The fact that we need a 2000K model with $\log g$ as high as 6.0 to reproduce the NaID line strength in component C and similar values for component B (Fig. 7) therefore simply indicates that these objects are very dusty, i.e. contain more dust than our handling of dust formation in current models allows for. Not only the NaID lines, but all optical atomic lines behave like this.

The extreme weakness of all atomic lines in the spectra of B and C therefore appears as a consequence of the presence of dust in suspension in their atmospheres. The difficulty to model the actual strength of lines suggests that some important dust opacity source has yet to be included into the models. Some of the opacity contributors left out for lack of cross-section data may have non-negligible effects. Or perhaps some types of grains can be porous, larger than assumed, or both.

For components B and C we then have the situation that the atomic lines prove sensitive more to the amount of dust included in the models than to gravity. Therefore the gravity of the two dusty companions B and C is difficult to ascertain from their spectra, and we have adopted a value of $\log g = 5.5 \pm 0.5$ from the predictions of the interior models for their respective effective temperatures when assuming solar metallicity and an age of 5 Gyr for the system.

6.2.4. Metallicity

The main indicators are the strength of the MgH band near 520 nm, and of the CaH bands near 620 nm, 640 nm, and 700 nm relative to the TiO band strengths, which ratio increases for lower metallicity. This is due to enhanced gas pressure and decreased TiO and VO absorption (double-metals) in metal-depleted atmospheres. Another indicator is the strength of the metal lines which increase relative to the "continuum" and become more broadened as metallicity decreases, and of which the more important ones are indicated in Figs. 2 and 3. We have found that the CaH bands are adequately reproduced only for solar or higher metallicity, while the MgH band strength seems then already overestimated. The atomic lines are quite well reproduced in the primary component when assuming solar metallicity, and those in the two faint components are even weaker than our metal-rich, dusty models would predict. These arguments together, although none of them is individually strong, argue against low metallicity, and we conclude that the metal content of the atmospheres of the components of LHS 1070 is likely to be close to solar.

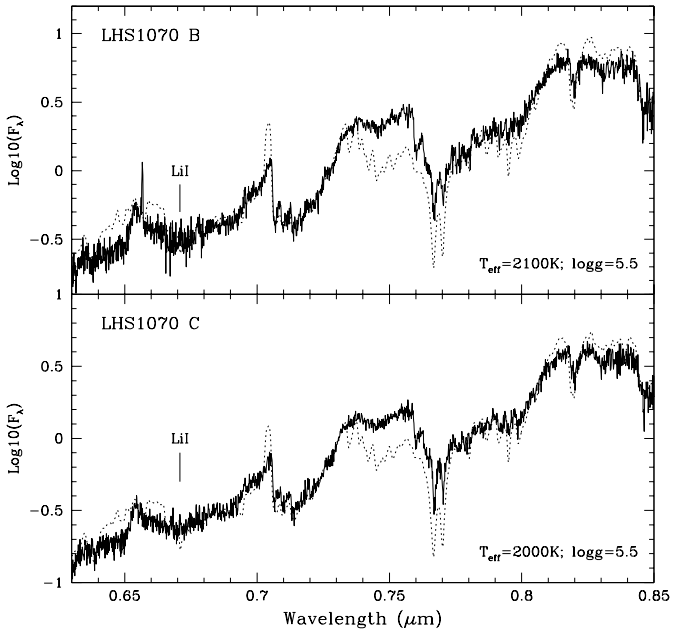

Fig. 7. Atmospheric models selected to fit the Na I-D lines in the cool components B and C. These, in comparison with Fig. 3, again demonstrate the effect of increased dust content on the strength of the alkali element lines (here the K I doublet). The models are not considered a realistic representation of the stars - they would require a distance as small as 4.8 pc to reproduce the observed fluxes.

6.2.5. Lithium abundance

The interest in this species comes from the fact that it is an indicator of youth in young stars and an indicator of substellar mass in low-mass objects (so-called "Lithium test", Magazzù et al. 1993, Basri 1998). As we see in Fig. 2, there is no evidence for the Lithium line at 670.9 nm in the spectra of components B and C. In the light of the "Lithium test" this excludes that these components could have substellar masses of less than $\approx$0.06 $M_\odot$.

However, the just discussed strong effects of dust concentration on the alkali lines in cool stellar atmospheres means that for such objects elemental abundance determination from equivalent line widths can be hazardous. This has implications

Table 8. Signs of activity in the components of LHS 1070

Spectral feature	Component A	B	C
UV emission	possible	yes	less
H_α, H_β, H_γ	yes	yes	no[1]
Na I D emission	yes	yes	no

[1] in spite of low F_λ of surrounding quasi-continuum

about the applicability of the Lithium test for substellarity in dusty red dwarfs: the absence of the Li I line at 6708A in a very dusty object does not necessarily mean it is a star or a transition object, but simply could show that its atmosphere is opaque with dust clouds. We have therefore to be very careful about conclusions drawn from the non-detectability of the Li I line in low-temperature objects.

In principle then it would be possible that the Li absorption line is quenched by the dust heating effects in component B's and C's atmospheres even though their lithium abundance is still high; then these components would have to be considered as brown dwarfs of less than 0.06 $M_\odot$. We do not propose that this actually is the case, because effective temperatures we derive for the faint companions (2400K,2300K) appear to exclude substellarity. But we want to take this example as a reminder of the intricacies of the apparently so simple Lithium test.

6.3. Activity

The main indicators of chromospheric activity are the presence and strength of the Balmer lines of hydrogen in emission, the presence of ultraviolet emission ($\lambda < 4000$Å), and emission cores of atomic resonance lines such as those of the Na I D lines at λ5890,5896 Å. The presence or absence of ultraviolet emission can be judged from our low resolution spectra in Figs. 4 and 5. Most of the absorption lines observed in our LHS1070 spectra are resonance transitions of alkali elements with cores formed in the uppermost layers of the photosphere. Chromospheric activity then fills up the cores of the lines. We probably see this effect in the Na I D lines of components A and B. We summarize the presence of indicators for non-photospheric activity in the three LHS1070 components in Table 8. While components A and B show chromospheric activity at a level typical for late M dwarfs, C has virtually none.

The two faintest components, B and C, form a close pair of very similar stars with differences in effective temperature of only 100 K and in mass of only ≈ 0.002 $M_\odot$, and with presumably the same age and metallicity. It is therefore surprising that these two stars should show such different levels of chromospheric activity. In common understanding those low-mass stars lacking activity are the ones lacking rotation. However, Basri & Marcy (1995) present the example of the rapidly rotating brown dwarf candidate BRI 0021-214 (M9,5+) which shows no Hα emission. They suggest that by some means magnetic activity may be increasingly quenched in M7 - M10 stars (a possible mechanism being that with decreasing mass and temperature the outward flux decreases and so could do the convective flux driving the activity). At present, it remains undecided if one of these mechanism, and if so, which one is responsible for the lack of activity in component C.

6.4. Appraisal

The new models with their physical treatment of dust condensation give substantial improvements in the representation of the spectra of cool M dwarfs like the components of the triple system LHS 1070. They are an important step forward in the attempt to understand these objects. But the topic is by no means closed. Certainly it will need a reliable value for the parallax and new infrared data to improve on the determination of the physical parameters. The present values for $T_{\rm eff}$, derived for a distance of 8.8 pc, may be slightly overestimated for that reason. In addition, a refined treatment of the dust effects may be necessary to obtain best fits to features and the overall spectrum for one and the same temperature. As a result, the values for the physical parameters given in this paper may have to be revised again, the changes probably being in the order of the given error bars.

In the introduction we asked the question how important settling of dust will be in cool atmospheres as function of spectral type. Unfortunately we could not answer this question based on the LHS1070 system alone, since components B and C are different in $T_{\rm eff}$ by only 100K, and component A shows no dust effects at all. However, we find that components B and C (the latter with spectral type L0) are the dustiest objects that we have been able to study thus far, i.e. dustier than the mid-L type dwarfs Kelu-1 (Ruiz et al. 1998) and GD165B (Kirkpatrick et al. 1999b), which themselves are far dustier than the T (= methane dominated spectrum) dwarf Gliese 229B (Oppenheimer et al. 1998). Perhaps this indicates that grains form larger and rain out more easily as $T_{\rm eff}$ decreases. However, it could mean instead that dust clouds are confined to thin layers of haze rather than extend, like their condensation zone, across most of the upper photosphere (as assumed in our simple models). Both of these possibilities cannot be modeled at this point without introducing additional parameters such as the typical radial extension of the cloud layers or the rate of gravitational settling for each grain type. While these can and will be explored in subsequent work, it becomes clear that the models will learn more of the diversity of brown dwarfs found and of their specific spectral characteristics than they ever did in the past. We used physical models to describe stellar atmospheres and derive their parameters. Now we need the observed wide variety of brown dwarfs to teach the models about the atmospheres, how dust clouds form and behave as a function of decreasing effective temperature and gravity.

7. Conclusion

We summarise and conclude:

(1) Based on our BVRI photometry and the updated Baraffe et al. (1998, 1999) combined interior and atmosphere models, components B and C of LHS 1070 do have masses close to

0.080 $M_\odot$. On the same grounds, component A has a somewhat higher mass of 0.10 $M_\odot$ - 0.11 $M_\odot$, and this result is essentially independent of the presence of its close companion, component D, recently discovered by Henry et al. (1999). We therefore consider Components B and C as *stars*, though of very low mass and at the end of the main sequence.

(2) It is in the mass range spanned by the components of LHS 1070 that we have a strong drop in the effective temperature of low-mass stars and the onset of dust formation in their atmospheres.

(3) The new models called "AMES-MT-Dusty", which include the formation of dust in cool regions of the stellar atmospheres, are able to describe the main photospheric features of the visible and far-red spectra of the components of LHS 1070.

(4) The apparent weakness of atomic lines in the two faint and dusty components B and C is explained by the presence of dust in suspension in their atmospheres which strongly heats the line forming layers. This quenching also applies to the Li I λ6709 absorption line and complicates the application of the "Lithium test" in cool objects.

(5) The spectrum of component A gives no clear clue with regard to the presence or absence of a cooler, unresolved object like component D.

(6) Judged from their spectra, the components of LHS 1070 have solar metallicity. Based on its high space motion, the age of the system should be several gigayears.

(7) The question remains to be answered whether the difference in activity between the otherwise very similar components B and C is due to the lower temperature of component C, due to slower rotation or due to some other effect.

Components C, B and D of LHS 1070 (in this order) will be the least luminous objects in the so-called "20-20-20" sample of nearby very low mass stars put together by Henry et al. (1999). The system LHS 1070 thus will largely determine what we will know about the end of the main sequence and the transition region to the brown dwarf regime. Therefore, dynamical masses for components B and C, for which first results should be available within a couple of years, are expected to provide significant new information. To this purpose, however, a definite value of the parallax for the system LHS 1070, free of possible effects of the three companions, has to be available.

This study will be followed, in a separate publication, by the analysis of the near-infrared spectral distribution (obtained from HST NICMOS spectra and photometry) and of mid-infrared photometry and spectrophotometry of the system (obtained from ISO observations).

Acknowledgements. We thank S. Casertano, W. Freudling and the staff at STScI and EDF for their continuing and friendly support of our work. In particular we want to mention Denise Taylor who did an excellent job in bringing to a good end our efforts to precisely determine the position of the objects in the HST frame. And we thank very much Michael Rosa for recalibrating the FOS spectra with the latest calibration files in August 1998. We are also grateful to G.M. Williger and A. van Teeseling for performing supporting ground-based photometry and spectroscopy, and to Bo Reipurth for taking a Schmidt plate of the object surroundings for astrometric purposes. H. Jahreiß was a constant and patient source of information on low-mass stars. It is a pleasure to thank I. Baraffe for making available the tabulations for the WFPC2 filters before publication. Support to France Allard for this work was provided by NASA through grant number GO-07415.01-96A from the Space Telescope Science Institute, which is operated by the Association of Universities for Research in Astronomy, Inc., under NASA contract NAS5-26555. Some of the calculations presented in this paper were performed at the "Centre National Universitaire Sud du Calcul" (CNUSC), the "Commissariat à l'Energie Atomique" (CEA), the University of Georgia computing facility UCNS, the San Diego Supercomputer Center (SDSC), the National Center for Supercomputing Applications (NCSA), and the Cornell Theory Center (CTC), with support from the american National Science Foundation, from the NERSC with support from the DoE. We thank all these institutions for a generous allocation of computer time. Further support came from NASA through grants 110-96LTSA, NAG5-3435, NAG5-3618, and NAG5-3619 (LTSA), as well as from CNRS through grants from INSU and ASPS. We thank J.Gizis for very helpful referee's comments.

Appendix A: derivation of colour corrections for the transformation from the HST VEGAMAG to the BVRI Johnson/Cousins systems for LHS 1070

Photometry carried out on the HST images can be expressed in terms of a synthetic flux-based magnitude system (so-called STMAG), or in terms of the HST WFPC2 flight system based on the Vega spectrum (so-called VEGAMAG). The two systems are easily related with each other, and in the remainder we will use only the VEGAMAG system.

In order to be able to compare the HST results with ground-based photometry and with empirical relations deduced from ground-based photometry, it is desirable to be able to convert the VEGAMAG system to the standard Landolt photometric system (i.e. Johnson UBV and Cousins RI filters). The paper by Holtzmann et al. (1995b) is the standard reference for such a transformation, but unfortunately it does not adequately cover the regime of very red colors which are characteristic of the components of LHS 1070.

In order to cope with this difficulty, we have used the HST Synphot package (available under IRAF) to establish our own transformations. Since the results might be useful to other authors, we present here some details of our work.

A total of 40 spectra from the Synphot database were used. These include: Vega (HST calibration spectrum); 29 stars from the Bruzual-Persson-Gunn-Stryker (BPGS) spectral atlas; 10 stars from the Jacoby-Hunter-Christian (JC) spectral atlas. Details on the above mentioned atlases are given in the Synphot User's Guide, Appendix B. The stars that we used include both dwarfs and giants, as well as some unclassified types which are presumably also giants (25, 12 and 2 in these classes respectively). The spectral types range from A0 to M8. Additionally, we included the 4 spectra measured on LHS 1070 itself (components A, B, C, and B+C since these two are not easily resolved from the ground). This can be done since the FOS spectra are independent from the photometry to which the resulting colour corrections are to be applied. These four spectra help to fill the diagram in the otherwise sparsely populated range of very red

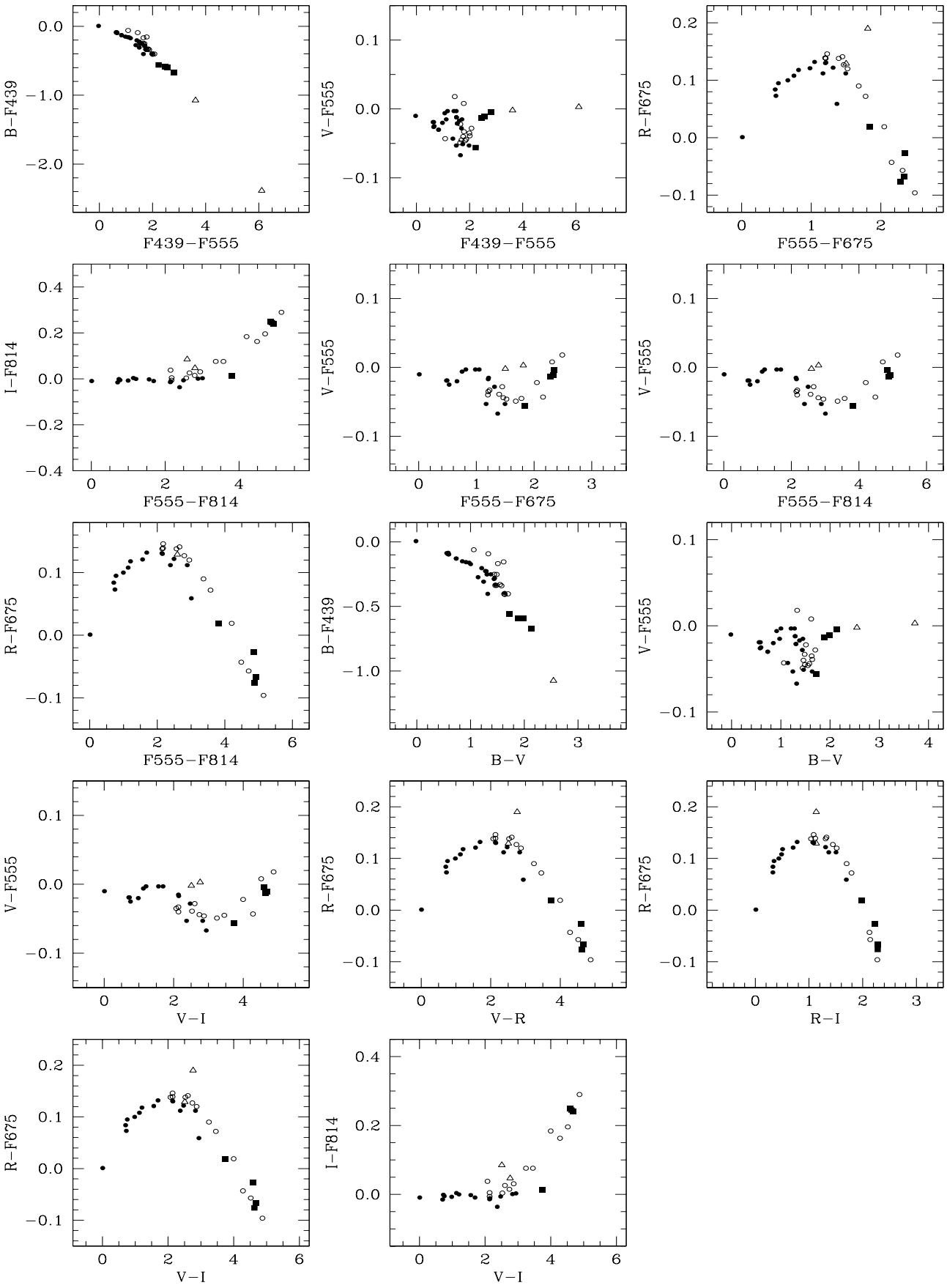

Fig. A.1. Synthetic colour corrections based on observed stellar spectra (for meaning of symbols see text).

Table A.1. Summary of synthetic photometry

Colors		Number of spectra		
Y	X	Total	Dwarfs	Giants
B-F439	F439-F555	44	25	13
V-F555	F439-F555	44	25	13
V-F555	F555-F675	34	15	13
V-F555	F555-F814	34	15	13
R-F675	F555-F675	34	15	13
R-F675	F555-F814	34	15	13
I-F814	F555-F814	34	15	13
B-F439	B-V	44	25	13
V-F555	B-V	44	25	13
V-F555	V-I	34	15	13
R-F675	V-R	34	15	13
R-F675	V-I	34	15	13
R-F675	R-I	34	15	13
I-F814	V-I	34	15	13

colours. In this way, we can also check that the results computed for the LHS 1070 spectra are in agreement with the general trends inferred from the set of the other measurements, and vice versa.

These 44 spectra were used to compute synthetic photometry in the VEGAMAG and Johnson/Cousins bands of interest, and from this we deduce the magnitude differences between corresponding filters of the two systems as function of the colour of the star, where for convenience of further use the colour is taken either from the VEGAMAG or the Johnson/Cousins system. A summary of the performed computations is given in Table A.1. We use the same nomenclature of the HST filters as in Table 1. Note that the JC stars have a limited coverage in the red part of the spectrum, and could not be used for computations involving the R,I and F675,F814 filters. Note also that, since we are calculating the magnitude *difference* between very similar filter passbands, the results are rather insensitive to uncertainties in the measured spectral fluxes.

The color-color diagrams giving the corrections from the VEGAMAG to the Landolt (Johnson/Cousins) systems are graphically presented in Fig. A.1, where the different symbols refer to dwarfs(filled circles), giants (open circles), unclassified stars, probably also giants (open triangles), and the components of LHS 1070, either individually or combined (filled squares). We can estimate the uncertainty of the transformation on the photometry of LHS 1070 from the scatter in these colour-colour relations to be less than a few percent.

References

Alexander D.R., Tamanai A., Allard F., Ferguson J. 1998, BAAS 192, 6716

Allard F. 1998, in "Brown dwarfs and extrasolar planets", R. Rebolo, E.L. Martín, M.R. Zapatero Osorio (eds.), ASP conference series, Vol. 134, p.370

Allard F., Hauschildt P.H., Baraffe I., Chabrier G. 1996, ApJ 465, L123

Allard F., Hauschildt P.H., Alexander D.R., Starrfield S. 1997, ARA&A 35, 137

Altena W.F. van, Lee J., Hoffleit D. 1995, The General Catalogue of Trigonometric Stellar Parallaxes, 4th ed., Yale University Obs. New Haven

Baraffe I., Chabrier G., Allard F., Hauschildt P.H. 1998, A&A 337, 403

Baraffe I., Chabrier G., Allard F., Hauschildt P.H. 1999, in: Very low-mass stars and brown dwarfs in stellar clusters and associations, proceedings of a conference in Los Cancajos, La Palma, May 11-15, 1998

Basri G. 1998. In: Brown dwarfs and extrasolar planets, R. Rebolo, E.L. Martín, M.R. Zapatero Osorio (eds.), ASP conference series, Vol. 134, p.394

Basri G., Marcy G.W. 1995, AJ 109, 762

Basri G., Allard F., Hauschildt P.H., Mohanty S. 1999. In: Very low-mass stars and brown dwarfs in stellar clusters and associations, proceedings of a conference in Los Cancajos, La Palma, May 11-15, 1998

Begemann B., Dorschner J., Henning Th. et al. 1997, ApJ 476, 199

Dorschner J., Begemann B., Henning Th., Jäger C., Mutschke H. 1995, A&A 300, 503

Graham J.A. 1982, PASP 94, 244

Grossman L. 1972, Geochim.Cosmochim. Acta 36, 597

Hauschildt P.H., Allard F., Baron E., Schweitzer A. 1999, ApJ 512, 377

Henry T.J., McCarthy T.W. 1993, AJ 106, 773

Henry T.J., Kirkpatrick J.D., Simons D.A. 1994, AJ 108, 1437

Henry T.J., Franz O.G., Wasserman L.H. et al., 1999, ApJ 512, 864

Holtzman J.A., Hester J.J., Casertano S. et al., 1995a, PASP 107, 156

Holtzman J.A., Burrows C.J., Casertano S. et al., 1995b, PASP 107, 1065

Kirkpatrick J.D. 1998, in Brown dwarfs and extrasolar planets, R. Rebolo, E.L. Martín, M.R. Zapatero Osorio, (eds.), ASP conference series Vol. 134, p. 405

Kirkpatrick J.D., Henry T.J., McCarthy Jr. D.W. 1991, ApJS 77, 417

Kirkpatrick J.D., Henry T.J., Simons D.A. 1995, AJ 109, 797

Kirkpatrick J.D., Reid I.N., Liebert J., et al., 1999a, ApJ 519,802

Kirkpatrick J.D., Allard F., Bida T., et al., 1999b, ApJ 519, 834

Landolt A.U. 1992, AJ 104, 340

Langhoff S.R. 1997, ApJ 481, 1007

Leggett S.K. 1992, ApJS 82, 351

Leggett S.K., Allard F., Hauschildt P.H., 1998, ApJ 509, 836

Leinert Ch., Weitzel N., Richichi A., Eckart A., Tacconi-Garman L.E. 1994, A&A 291, L47

Leinert Ch., Woitas J., Allard F., Richichi A., Jahreiß H. 1998, in: Brown dwarfs and extrasolar planets, R. Rebolo, E.L. Martin and M.R. Zapatero Osorio (eds.), ASP Conference Series Volume 134, San Francisco, p. 203

Magazzù A., Martín E.L., Rebolo R., 1993, ApJ 404, L17

Martín E.L., Rebolo R., Zapatero-Osorio M.R. 1996, ApJ 469, 706

Martín E.L., Basri G., Delfosse X., Forveille T. 1997, A&A 327, L29

Mathis J.S., Rumpl W., Nordsieck K.H. 1977, ApJ 217, 425

Miller S., Tennyson J., Jones H.R.A., Longmore A.J. 1994, in "Molecules in the Stellar Environment", U.G. Jørgensen ed., Lecture Notes in Physics, Springer-Verlag Berlin/Heidelberg, p. 296

Nakajima T., Oppenheimer B.R., Kulkarni S.R. et al. 1995, Nature 378, 463

Oppenheimer B.R., Kulkarni S.R., Matthews K., Nakajima T. 1995, Science 270, 1478

Oppenheimer B.R., Kulkarni S.R., Matthews K., van Kerkwijk M.H. 1998, ApJ 502, 932

Partridge H., Schwenke D.W. 1997, J. Chem. Phys. 106, 4618

Ruiz M.T., Leggett S.K., Allard F., 1998, ApJ 491, L107

Schweitzer A., Hauschildt P.H., Allard F., Basri G. 1997, MNRAS 283, 821
Schwenke D.W. 1998, in "Chemistry and Physics of Molecules and Grains in Space". Faraday Discussions No.109. The Faraday Division of the Royal Society of Chemistry, London, p. 321
Sharp C.M., Huebner W.F. 1990, ApJS 72, 417
Tinney C.G., Delfosse X., Forveille T., Allard F., 1998, A&A 338, 1066
Tsuji T., Ohnaka K., Aoki W. 1996a, A&A 305, L1
Tsuji T., Ohnaka K., Aoki W., Nakajima T. 1996b, A&A 308, L29
Whitmore B., Heyer I. 1997, Instrument Science Report WFPC2 97-08, available at http://www.stsci.edu/ftp/instrument_news/WFPC2/wfpc2_bib.html

Note added in proof: Recently, Martín et al. (ApJ Letters, accepted) discovered that the nearby M2 dwarf Gliese 569 also has two very faint companions, separated among them by 0.1", with estimated masses at or slightly below the hydrogen burning limit. As for LHS 1070, this constellation will allow to determine dynamical masses for the two faint components. The orbital period of this ylose pair is estimated to ≈ 3 years.